Chapter 4
Monolayer $PtSe_2$

Abstract Single-layer transition-metal dichalcogenides (TMDs) attract considerable attention due to their interesting physical properties and potential applications. Here, we demonstrate the epitaxial growth of high-quality monolayer platinum diselenide ($PtSe_2$), a new member of the layered TMDs family, by a single step of direct selenization of a Pt(111) substrate. A combination of atomic-resolution experimental characterizations and first-principles theoretic calculations reveals the atomic structure of the monolayer $PtSe_2$/Pt(111). Angle-resolved photoemission spectroscopy measurements confirm for the first time the semiconducting electronic structure of monolayer $PtSe_2$ (in contrast to its semimetallic bulk counterpart). The photocatalytic activity of monolayer $PtSe_2$ film is evaluated by a methylene-blue photodegradation experiment, demonstrating its practical application as a promising photocatalyst. Moreover, circular polarization calculations predict that monolayer $PtSe_2$ also has potential applications in valleytronics.

Keywords $PtSe_2$ · Transition metal dichalcogenides · Atomic structure · Electronic property · Photocatalysis · Valleytronics

4.1 Background

As discussed in Chap. 1, layered transition-metal dichalcogenides (TMDs) with the general formula MX_2, where M represents a transition metal from groups 4–10 and X is a chalcogen (S, Se, or Te), received significant attention in the last dozen years due to their intriguing physical properties for both fundamental research and potential applications in electronics, optoelectronics, spintronics, catalysis, and so on. Depending on the coordination environment and oxidization state of the transition metal, layered TMDs can be metals, semiconductors, and insulators and thus show various physical properties. Recent investigations of MX_2 have resulted in discoveries of dramatically different electronic structures at the monolayer limit compared to the bulk materials due to quantum confinement effects. For example, while pushing from bulk to monolayer, MoS_2 and $MoSe_2$ show an indirect-to-direct bandgap transition [1–4]. With these exciting findings, experimental research efforts so far have been mainly focused on prototypical semiconducting MX_2 with group VIB transition

© Springer Nature Singapore Pte Ltd. 2020

L. Li, *Fabrication and Physical Properties of Novel Two-dimensional Crystal Materials Beyond Graphene: Germanene, Hafnene and $PtSe_2$*, Springer Theses,
https://doi.org/10.1007/978-981-15-1963-5_4

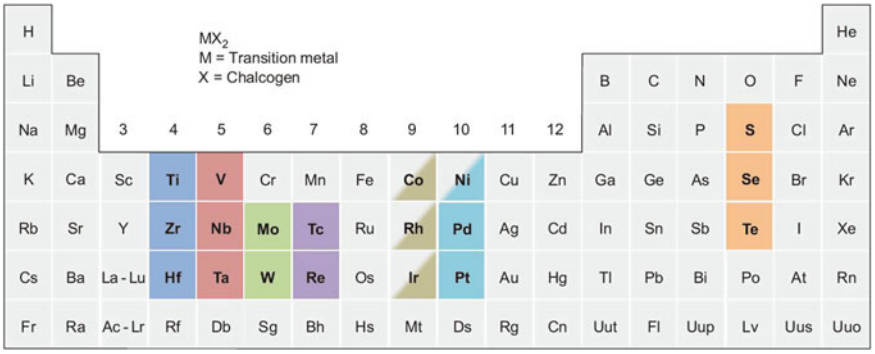

Fig. 4.1 Summary of about 40 different layered MX_2 compounds, which are highlighted. Partial highlights for Co, Rh, Ir and Ni indicate that only some of the dichalcogenides form layered structures. Reprinted with permission from Ref. [6], © 2013 Springer Nature

metals (M = Mo, W). Note, however, that about 40 different MX_2 compounds can form stable, 2D single-layer TMDs structures [5, 6], as summarized in Fig. 4.1. In the large family of layered TMDs, many other promising single-layer TMDs and related quantum defined properties remain to be explored experimentally. For example, $IrTe_2$ and 1T-TaS_2 exhibit novel low-temperature phenomena including superconductivity and charge density wave [7, 8]; bulk ReS_2 shows monolayer behavior due to electronic and vibrational decoupling [9]. These interesting properties motivate considerable interest in exploring other promising TMDs materials, such as group 10 TMDs, which have rarely been reported.

Reliable preparation of ultra-thin 2D TMDs is the essential step for exploring their properties and applications. Among various production methods, chemical vapor deposition (CVD) and CVD analogs are the most important approaches of bottom-up synthesis. As described in Sect. 1.3.4.2, MX_2 growth using CVD-related methods usually involves two components containing M and X as precursors, which increases experimental steps and complexities.

4.2 Growth and Atomic Structure

In this chapter, we report epitaxial growth of monolayer $PtSe_2$ - a heretofore-unexplored member of the single-layer TMDs family—on a Pt substrate by direct "selenization" [10], an analog of direct oxidation. In contrast to conventional fabrication methods of MX_2 by exfoliation or chemical vapor deposition, the present route toward a monolayer dichalcogenide is very straightforward: only one element, Se, is deposited on a Pt(111) substrate, and then the sample is annealed to ~200 °C to obtain epitaxial $PtSe_2$ films, as illustrated in Fig. 4.2a.

The growth of $PtSe_2$ thin films was monitored by in situ X-ray photoelectron spectroscopy (XPS). Figure 4.2b shows the XPS spectra of the Se 3d core level during

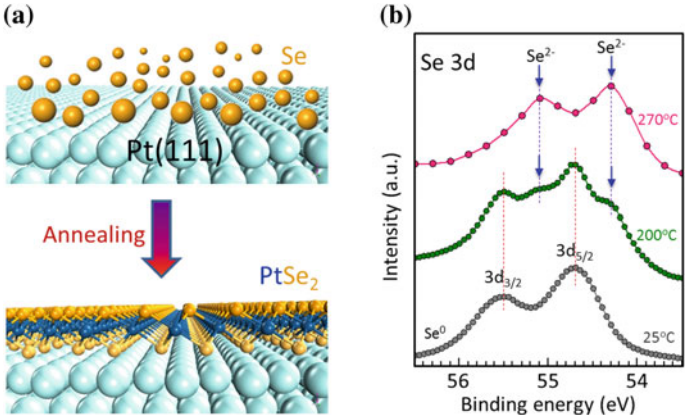

Fig. 4.2 **a** Schematic illustration of synthesizing $PtSe_2$ monolayer by a single step of direct selenization of a Pt(111) substrate. The Pt spheres with different colors and sizes are used just to differentiate the Pt atoms in the Pt(111) substrate and in the $PtSe_2$ sublayer. **b** XPS measurements for the binding energies of Se during $PtSe_2$ growth demonstrating the formation of $PtSe_2$ at 270 °C. The blue arrows indicate the peak positions (55.19 and 54.39 eV) corresponding to the binding energy of Se^{2-}. The Se^0 peaks (at 55.68 and 54.80 eV) are dominant at 25 °C, whereas at 200 °C the peaks in the curve indicate the coexistence of Se^0 and Se^{2-}. Reprinted with permission from Ref. [10], © 2015 ACS

$PtSe_2$ growth. When Se-deposited Pt(111) substrate is annealed to 200 °C, two new peaks appear at binding energies of 55.19 and 54.39 eV (labeled by the blue arrows), which can be explained by a change in the chemical state of Se from Se^0 to Se^{2-}, corresponding to the selenization process of the sample. Further annealing of the sample to 270 °C results in the disappearance of Se^0 peaks (at 55.68 and 54.80 eV) and the dominance of Se^{2-} peaks, indicating full crystallization and complete formation of $PtSe_2$ films.

To obtain the structural information on the as-grown epitaxial films, we observed the samples by LEED. Figure 4.3a shows a LEED pattern. Hexagonal diffraction spots from $PtSe_2$ (red circles) are observed to have the same orientation as those from the Pt(111) substrate (blue circles), suggesting a rotational-domain-free growth. A (3×3) diffraction pattern of the epitaxial $PtSe_2$ film is clearly identified, which corresponds to a well-defined moiré superstructure arising from the lattice mismatch between the $PtSe_2$ film and Pt(111) substrate. Furthermore, identical LEED patterns were observed on the entire sample surface (4 mm × 4 mm in size), indicating the growth of a large-area, homogeneous, and high-quality film.

To investigate the atomic structure of the $PtSe_2$ film, we performed STM studies. Figure 4.3b is a large-scale STM image with a well-ordered moiré pattern of $PtSe_2$ thin film on Pt(111). The periodicity of this moiré pattern is about 11.1 Å, four times the lattice constant of Pt(111). Figure 4.3c shows an atomic-resolution image of the area indicated by the white square in Fig. 4.3b, revealing hexagonally arranged protrusions with an average lattice constant of $a_1 = 3.7$ Å, which agrees perfectly

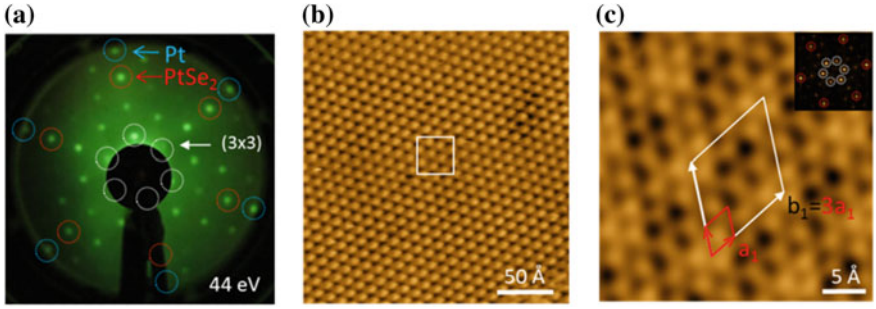

Fig. 4.3 **a** LEED pattern of $PtSe_2$ films formed on the Pt substrate. The blue, red, white circles indicate the diffraction spots from the Pt(111) lattice, $PtSe_2$ thin film, and (3 × 3) superstructure with respect to $PtSe_2$, respectively. **b** Large-scale STM image (U = −1.9 V, I = 0.12 nA) shows the moiré pattern of $PtSe_2$ thin film on Pt(111). The white rectangle marks the size of the close-up image in (**c**). **c** Atomic-resolution STM image (U = −1.0 V, I = 0.12 nA) of single-layer $PtSe_2$ showing the hexagonal lattice of Se atoms in the topmost sublayer of the $PtSe_2$ sandwich-type structure. A (3 × 3) moiré superstructure is visible. The red and white rhombi denote the unit cell of the $PtSe_2$ lattice and (3 × 3) superlattice, respectively. The inset displays the FFT pattern corresponding to $PtSe_2$ and the superstructure. Adapted with permission from Ref. [10], © 2015 ACS

with the interatomic spacing of Se atoms in the (0001) basal plane of bulk $PtSe_2$. Therefore, we interpret the hexagonal protrusions in Fig. 4.3c to be the Se atoms in the topmost Se plane of a $PtSe_2$ film. A regular (3 × 3) moiré superstructure with respect to the $PtSe_2$ lattice is then established, with a periodicity of $b_1 = 3a_1 \cong 11.1$ Å (labeled by the white rhombus). The orientation of the moiré pattern is aligned with that of the $PtSe_2$ lattice. This is in agreement with the LEED observation (Fig. 4.3a), where the diffraction spots of the (3 × 3) superlattice are in line with those of the $PtSe_2$ lattice. Based on LEED and STM measurements, the moiré pattern can be explained as the (3 × 3) $PtSe_2$ supercells located on the (4 × 4) Pt(111) atoms.

To gain further insight into interfacial features of the $PtSe_2$/Pt(111) sample, we performed a cross-section high-angle annular-dark-field (HAADF) STEM study. A Z-contrast image of the $PtSe_2$/Pt(111) interface is shown in Fig. 4.4a. One bright layer combined with two dark layers observed on the topmost surface suggests a Se–Pt–Se sandwich configuration (as indicated by a model diagram superimposed in Fig. 4.4a). The atomically resolved bulk Pt substrate lattice with an experimentally measured interlayer spacing of 2.28 Å served as a reference for calibrating other spacing measurements. After the calibration, the spacing between the Se sublayers in the Se–Pt–Se sandwich is found to be 2.53 Å, which is in agreement with the calculated value in single-layer $PtSe_2$, as displayed in Fig. 4.4b. These atomic-scale cross-section data obtained by STEM further verify that the fabricated structure is indeed a single-layer $PtSe_2$ film on the Pt(111) substrate.

The combination of LEED, STM, and STEM studies indicates a (3 × 3) single-layer $PtSe_2$ on a (4 × 4) Pt(111) structure. We then carried out DFT calculations based on this structure. The simulated STM image is shown in Fig. 4.4c, in which the overall features of the experimental STM image (Fig. 4.3c) are well reproduced.

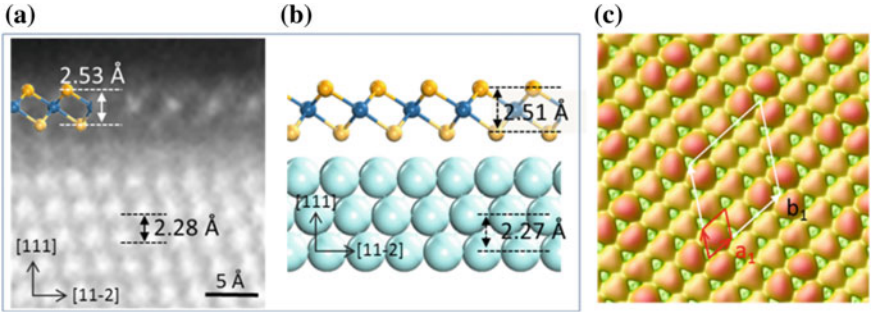

Fig. 4.4 **a** Atomic-resolution STEM Z-contrast image of the $PtSe_2$/Pt(111) interface along the [110] zone axis. A $PtSe_2$ single layer over the Pt(111) substrate is resolved at atomic scale with a model diagram overlaid for clarity. **b** The relaxed model. The blue and orange spheres represent Pt atoms and Se atoms, respectively. **c** Simulated STM image (U = −1.0 V) based on the calculated atomic structure in (**b**) is consistent with the experimental observation in Fig. 4.3c. Adapted with permission from Ref. [10], © 2015 ACS

Only the hexagonally arranged Se atoms in the topmost sublayer of monolayer $PtSe_2$ are imaged. The remarkable agreement between the STM simulation and experimental STM observation strongly supports our conclusions and thus demonstrates the successful growth of a highly crystalline $PtSe_2$ monolayer.

4.3 Electronic Structure

Having grown highly crystalline single-layer $PtSe_2$, we investigated its electronic energy band structure by ARPES. Figure 4.5a shows ARPES data measured along the high symmetry direction K-Γ-M-K in the hexagonal Brillouin zone at a photon energy of 21.2 eV. Data taken at other photon energies show the same dispersion, confirming the 2D character of the monolayer $PtSe_2$. Second-derivative spectra of raw experimental band structures (Fig. 4.5a) are depicted in Fig. 4.5b to enhance the visibility of the bands. Here, the top of the valence band is observed to be at −1.2 eV at the Γ point and the conduction band is above the Fermi level, indicating that monolayer $PtSe_2$ is a semiconductor. It is quite different from the bulk $PtSe_2$, which-according to calculations-is a semimetal. A direct comparison between the ARPES spectrum (Fig. 4.5b) and the calculated band structure (green dotted lines in Fig. 4.5b) shows excellent quantitative agreement. Combining the ARPES spectra with DFT calculations, we confirm that we have synthesized a single-layer $PtSe_2$ and that the epitaxial $PtSe_2$ essentially has the same electronic properties as the free-standing single-layer $PtSe_2$. For the first time, the band structure of monolayer $PtSe_2$ films has been determined experimentally.

The semimetal-to-semiconductor transition was revealed by DFT-LDA calculations. As shown in Fig. 4.5c, the band structure and density of state (DOS) suggest

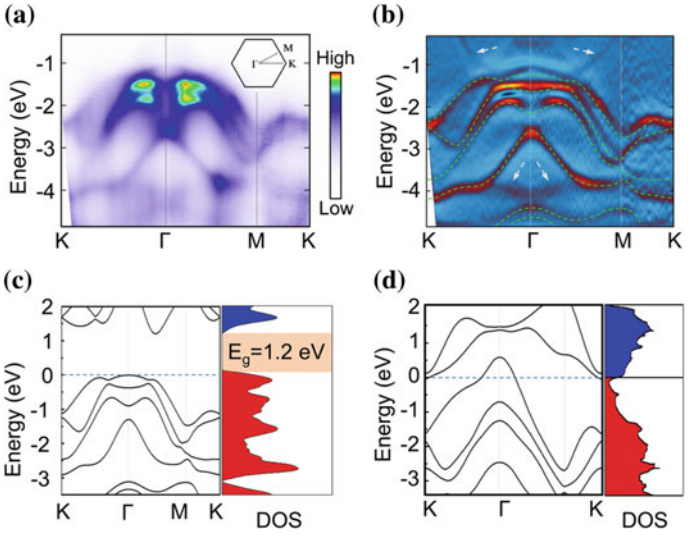

Fig. 4.5 ARPES spectra and valence bands of single-layer $PtSe_2$. **a** ARPES spectra obtained on the monolayer $PtSe_2$ on Pt(111). The high symmetry directions are shown in the inset. **b** Second-derivative spectra of the raw ARPES data in (**a**). The calculated valence bands, superimposed as green dashed lines, are in excellent agreement with the experimental data. The bands marked by white arrows are from the Pt substrate. **c**, **d** Theoretically calculated band structure and density of states of monolayer $PtSe_2$ and bulk $PtSe_2$, respectively. Reproduced with permission from Ref. [10], © 2015 ACS

single-layer $PtSe_2$ is a semiconductor with an energy gap of 1.20 eV (2.10 eV bandgap is predicted from GW calculation [11]). As a comparison, the band structure and DOS of bulk $PtSe_2$ are plotted in Fig. 4.5d, which confirm that bulk $PtSe_2$ is semimetallic [12, 13]. Actually, bilayer $PtSe_2$ remains a semiconductor, but the energy gap decreases to 0.21 eV. Starting from a trilayer, $PtSe_2$ becomes semimetallic, as shown in Fig. 4.6. Therefore, only single-layer $PtSe_2$ is a semiconductor with a sizeable bandgap.

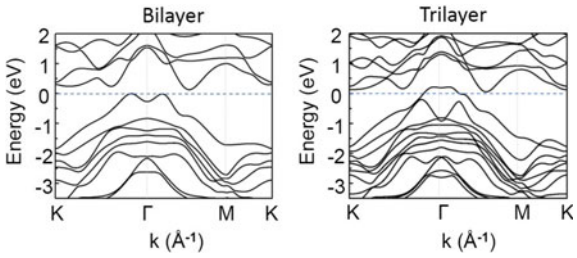

Fig. 4.6 Calculated band structures of free-standing bi- and tri-layer $PtSe_2$. Reproduced with permission from Ref. [10], © 2015 ACS

4.4 Photocatalytic Properties

The opening of a sizable bandgap within the range of visible light makes monolayer $PtSe_2$ potentially suitable for optoelectronics and photocatalysis. We explored the photocatalytic properties of monolayer $PtSe_2$ by the degradation of methylene blue (MB) aqueous solution, which serves as a typical indicator of photocatalytic reactivity [14, 15].

4.4.1 Experimental Setups

Figure 4.7a displays the schematic diagram of photocatalytic experiments. The photocatalytic activity of as-prepared monolayer $PtSe_2$ films was tested by catalytic degradation of methylene blue serving as a standard model dye under visible-light irradiation at room temperature. The ultraviolet/visible-light source was a 150 W Xe lamp located at a distance of 15 cm above the solution. A set of appropriate cut-off filters was applied to determine illumination wavelength and ensured that the photocatalytic reaction took place just under visible light. The as-prepared monolayer $PtSe_2$ films were exfoliated from the Pt(111) substrate by ultra-sonication in aqueous solution. The Pt(111) crystal was picked out from the solution to avoid its possible influence on the photocatalytic activity. Then MB molecules and ethanol (0.01 mL)

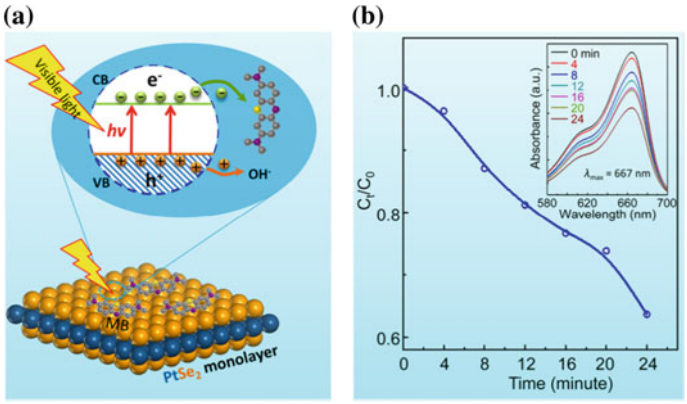

Fig. 4.7 Photocatalytic activity of a single-layer $PtSe_2$ film. **a** Schematic diagram of the photocatalytic degradation of methylene blue (MB) molecules. Electrons and holes are excited by visible-light irradiation of epitaxial $PtSe_2$ monolayer films. The MB degradation by photo-induced electrons demonstrates the photocatalytic activity of $PtSe_2$ monolayer films. **b** Time trace of the normalized concentration (C_t/C_0, where C_t and C_0 are the MB concentrations at time t min and 0 min, respectively) of the absorbance at a wavelength of 667 nm, the main absorbance peak of MB. The inset shows the UV-vis absorption spectra of MB, recorded at time intervals of 4 min. Reproduced with permission from Ref. [10], © 2015 ACS

were added to the solution containing peeled $PtSe_2$ monolayers. Before the photocatalytic reaction, the solution was kept in darkness for one hour in order to achieve an adsorption-desorption equilibrium between the $PtSe_2$ film and MB molecules. After that, the suspension was exposed to visible-light irradiation. At time intervals of 4 min, solution samples were collected and their absorbance was measured by a commercial ultraviolet-visible (UV-vis) spectrophotometer. Accordingly, the intensity changes of characteristic absorbance peaks of the MB molecules were recorded. The photocatalytic performance of $PtSe_2$ monolayers was thus evaluated by the time-dependent degradation rate C_t/C_0, as exhibited in Fig. 4.7b.

4.4.2 Photocatalytic Characterizations

The MB molecules adsorbed on the $PtSe_2$ films are degraded by electrons that are excited by visible light. The time-dependent degradation of MB with a single layer $PtSe_2$ catalyst was monitored by checking the decrease in the intensities of characteristic absorbance peaks of the MB molecules. As we can see in Fig. 4.7b, the photodegradation portion of MB molecules reached 38% after visible-light irradiation for 24 min. This rate is about four times faster than the rate obtained using $PtSe_2$ nanocrystals [16, 17], putting single-layer $PtSe_2$ in the same class as nitrogen-doped TiO_2 nanoparticles for photocatalysis [18, 19].

4.5 Valleytronics

With the existence of an energy gap in the single-layer $PtSe_2$, optical excitations can occur between the Γ point and the valley point along the Γ-M direction. This is reminiscent of the recently discovered valley-selective circular dichroism in MoS_2 by circularly polarized light [20–22]. To explore this possibility, we calculated the degree of circular polarization of free-standing single-layer $PtSe_2$. The calculated circular polarization due to the direct interband transition between the top of the valence band (VB) to the bottom of the conduction band (CB) is shown in Fig. 4.8a. It shows significant circular dichroism polarization along the M-K direction and near the Γ point. In view of the indirect energy gap, this process can be assisted by lattice vibrations. It is noteworthy that the circular dichroism polarization not only exists in the transition between the top of the VB and the bottom of the CB, it also exists in transitions to higher energy levels. Circular dichroism polarization due to transitions from the vicinity of the VB to the vicinity of the CB can be clearly seen in Figs. 4.8b–d. Due to this significant circular polarization, in the presence of a nonvanishing in-plane electric field, the anomalous charge current driven by the Berry curvature would flow to the opposite edges, leading to a valley polarized current and the resulting quantum valley Hall effect [23, 24].

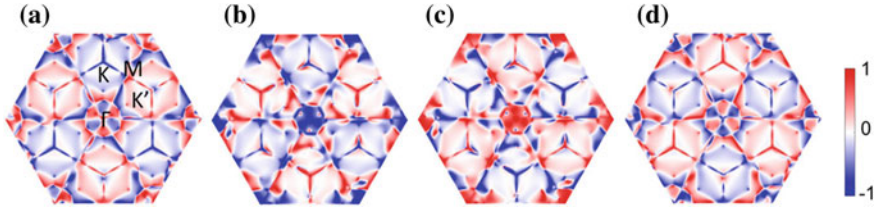

Fig. 4.8 Momentum dependence of circular polarization of single-layer $PtSe_2$. **a–d** represent the calculated circular polarization due to the direct interband transition from the top of the valence band (VB1) to the bottom of the conduction band (CB1), from VB1 to the higher conduction band (CB2), from the lower valence band (VB2) to CB1, and from VB2 to CB2, respectively. Significant circular dichroism polarization exists along the M-K direction and near the Γ point. Reproduced with permission from Ref. [10], © 2015 ACS

4.6 Summary and Outlook

We have successfully fabricated high-quality, single-crystalline, monolayer $PtSe_2$ films, a new member of the TMDs family, through a single-step, direct selenization of a Pt(111) substrate at a relatively low temperature (∼270 °C).

(1) Characterizations by LEED, STM, STEM, and DFT calculations elucidated both in-plane and vertical monolayer structures with atomic resolution.
(2) The ARPES measurements and their agreement with calculations revealed the semiconducting electronic structure of the single-layer $PtSe_2$.
(3) Together with the photocatalytic performance observed experimentally, monolayer $PtSe_2$ shows promise for potential applications in optoelectronics and photocatalysis.
(4) The circular polarization of monolayer $PtSe_2$ in momentum space indicates a promising potential for valleytronic devices.
(5) Our studies are a significant step forward in expanding the family of single-layer semiconducting TMDs and exploring the application potentials of ultra-thin TMDs in photoelectronic and energy-harvesting devices.

References

1. Splendiani A et al (2010) Emerging photoluminescence in monolayer MoS_2. Nano Lett 10:1271–1275. https://doi.org/10.1021/nl903868w
2. Eda G et al (2011) Photoluminescence from chemically exfoliated MoS_2. Nano Lett 11:5111–5116. https://doi.org/10.1021/nl201874w
3. Tongay S et al (2012) Thermally driven crossover from indirect toward direct bandgap in 2D semiconductors: $MoSe_2$ versus MoS_2. Nano Lett 12:5576–5580. https://doi.org/10.1021/nl302584w
4. Zhang Y et al (2014) Direct observation of the transition from indirect to direct bandgap in atomically thin epitaxial $MoSe_2$. Nat Nanotechnol 9:111–115. https://doi.org/10.1038/Nnano.2013.277

5. Ataca C, Sahin H, Ciraci S (2012) Stable, single-layer MX_2 transition-metal oxides and dichalcogenides in a honeycomb-like structure. J Phys Chem C 116:8983–8999. https://doi.org/10.1021/jp212558p
6. Chhowalla M et al (2013) The chemistry of two-dimensional layered transition metal dichalcogenide nanosheets. Nat Chem 5:263–275. https://doi.org/10.1038/nchem.1589
7. Sipos B et al (2008) From Mott state to superconductivity in 1T-TaS_2. Nat Mater 7:960–965. https://doi.org/10.1038/nmat2318
8. Yang JJ et al (2012) Charge-orbital density wave and superconductivity in the strong spin-orbit coupled $IrTe_2$:Pd. Phys Rev Lett 108:116402. https://doi.org/10.1103/PhysRevLett.108.116402
9. Tongay S et al (2014) Monolayer behaviour in bulk ReS_2 due to electronic and vibrational decoupling. Nat Commun 5:3252
10. Wang YL et al (2015) Monolayer $PtSe_2$, a new semiconducting transition-metal-dichalcogenide, epitaxially grown by direct selenization of Pt. Nano Lett 15:4013–4018. https://doi.org/10.1021/acs.nanolett.5b00964
11. Zhuang HLL, Hennig RG (2013) Computational search for single-layer transition-metal dichalcogenide photocatalysts. J Phys Chem C 117:20440–20445. https://doi.org/10.1021/jp405808a
12. Guo G, Liang W (1986) The electronic structures of platinum dichalcogenides: PtS_2, $PtSe_2$ and $PtTe_2$. J Phys C: Solid State Phys 19:995
13. Dai D et al (2003) Trends in the structure and bonding in the layered platinum dioxide and dichalcogenides PtQ_2 (Q=O, S, Se, Te). J Solid State Chem 173:114–121
14. Houas A et al (2001) Photocatalytic degradation pathway of methylene blue in water. Appl Catal B 31:145–157
15. Costi R, Saunders AE, Elmalem E, Salant A, Banin U (2008) Visible light-induced charge retention and photocatalysis with hybrid CdSe-Au nanodumbbells. Nano Lett 8:637–641
16. Wilson JA, Yoffe AD (1969) The transition metal dichalcogenides discussion and interpretation of the observed optical, electrical and structural properties. Adv Phys 18:193
17. Ullah K et al (2014) Synthesis and characterization of novel $PtSe_2$/graphene nanocomposites and its visible light driven catalytic properties. J Mater Sci 49:4139–4147
18. Asahi R, Morikawa T, Ohwaki T, Aoki K, Taga Y (2001) Visible-light photocatalysis in nitrogen-doped titanium oxides. Science 293:269–271. https://doi.org/10.1126/science.1061051
19. Gole JL, Stout JD, Burda C, Lou YB, Chen XB (2004) Highly efficient formation of visible light tunable $TiO_{2-x}N_x$ photocatalysts and their transformation at the nanoscale. J Phys Chem B 108:1230–1240. https://doi.org/10.1021/jp.030843n
20. Cao T et al (2012) Valley-selective circular dichroism of monolayer molybdenum disulphide. Nat Commun 3:887
21. Mak KF, He K, Shan J, Heinz TF (2012) Control of valley polarization in monolayer MoS_2 by optical helicity. Nat Nanotechnol 7:494–498. https://doi.org/10.1038/nnano.2012.96
22. Zeng H, Dai J, Yao W, Xiao D, Cui X (2012) Valley polarization in MoS_2 monolayers by optical pumping. Nat Nanotechnol 7:490–493. https://doi.org/10.1038/nnano.2012.95
23. Rycerz A, Tworzydło J, Beenakker C (2007) Valley filter and valley valve in graphene. Nat Phys 3:172–175
24. Xiao D, Yao W, Niu Q (2007) Valley-contrasting physics in graphene: magnetic moment and topological transport. Phys Rev Lett 99:236809